Journal of Materials Chemistry

Cite this: J. Mater. Chem., 2012, 22, 13947

www.rsc.org/materials

PAPER

Chemically derived graphene–metal oxide hybrids as electrodes for electrochemical energy storage: pre-graphenization or post-graphenization?†

Cheng-Meng Chen,[ab] Qiang Zhang,[bc] Jia-Qi Huang,[c] Wei Zhang,[b] Xiao-Chen Zhao,[bf] Chun-Hsien Huang,[be] Fei Wei,[c] Yong-Gang Yang,[a] Mao-Zhang Wang[a] and Dang Sheng Su*[bd]

Received 21st November 2011, Accepted 9th May 2012
DOI: 10.1039/c2jm16042k

The introduction of a secondary phase is an efficient and effective way to improve the electrochemical performance of graphene towards energy storage applications. Two fundamental strategies including pre-graphenization and post-graphenization were widely employed for graphene-based hybrids. However, there is still an open question of which way is better. In this contribution, we investigated the differences in the structure and electrochemical properties of pre- and post-graphenized graphene–SnO_2 hybrids. The pre-graphenization is realized by synthesis of thermally reduced graphene and subsequent impregnation of SnO_2, while the post-graphenization is realized by introducing a Sn-containing phase onto GO sheets followed by chemical reduction. The pre-graphenization process provides a large amount of pores for ion diffusion, which is of benefit for loading of SnO_2, fast ion diffusion for supercapacitors, and higher capacity for Li-ion batteries, but poor stability, while the post-graphenization process offers compact graphene and good interaction between the SnO_2 and graphene, which provides stable structure for long term stability for supercapacitor and Li-ion battery use.

1. Introduction

Advanced energy storage and conversion is an important issue for a sustainable development of our society. Electrochemical energy storage devices, such as supercapacitors and batteries, are playing a core role in balancing the energy generated by engines, solar and wind power. Supercapacitors, or electrochemical capacitors, are energy storage devices that store charges electrostatically through the reversible adsorption/desorption of ions in the electrolyte onto active materials,[1,2] while Li-ion batteries, which consist of two electrodes that are capable of reversibly hosting Li in ionic form,[3] are widely used for consumer electronics, power management, and hybrid electric vehicles. However, the energy density or power density of the two systems still needs to be improved for demanding applications. Exploring advanced electrode materials is one of the most straightforward approaches to improve the efficiency of electrochemical energy storage systems.

The element carbon is a very flexible choice for building electrochemical energy storage devices.[4] Graphite, hard carbon, glassy carbon, carbon black, mesocarbon microbead, activated carbon, and mesoporous carbon have been widely utilized in various energy storage systems.[5] Carbon nanotubes have been applied as an electric conductive additive for Li-ion batteries.[6] Graphene, the two-dimensional carbon crystal lattice with excellent electronic conductivity, optical transparency, mechanical strength, inherent flexibility, and huge theoretical surface area, has been considered a novel and portable nano-carbon component for electrodes of energy storage devices.[7–9] However, the irreversible aggregation of graphene sheets always creates more void units and masks active sites for pseudo-capacitor or Li-intercalation. Thus, metal oxides (*e.g.* RuO_2,[10] MnO_2,[2,11] Co_3O_4,[12] NiO,[13] SnO_2,[14–16] Fe_3O_4 (ref. 17)), conductive polymers (*e.g.* PANI,[18] PPy[19]) or nanocarbon (*e.g.* carbon nanotube[20]) are introduced as secondary phases that serve as "spacers" to avoid the re-stacking of graphene, provide pseudo-active centres for supercapacitors, or host storage materials for Li-ion batteries.

[a]*Key Laboratory of Carbon Materials, Institute of Coal Chemistry, Chinese Academy of Sciences, 27 Taoyuan South Road, Taiyuan 030001, China*
[b]*Department of Inorganic Chemistry, Fritz Haber Institute of the Max Planck Society, Faradayweg 4-6, Berlin 14195, Germany. E-mail: dangsheng@fhi-berlin.mpg.de*
[c]*Beijing Key Laboratory of Green Reaction Engineering and Technology, Department of Chemical Engineering, Tsinghua University, Beijing 100084, China*
[d]*Catalysis and Materials Division, Shenyang National Laboratory for Materials Science, Institute of Metal Research, Chinese Academy of Sciences, 72 Wenhua Road, Shenyang 110016, China*
[e]*Department of Biomedical Engineering and Environmental Sciences, National Tsing-Hua University, Hsinchu 30013, Taiwan*
[f]*State Key Laboratory of Catalysis, Dalian Institute of Chemical Physics, Chinese Academy of Science, PO Box 110, Dalian 116023, China*
† Electronic supplementary information (ESI) available: The performance of pure TRG and CRG as anode materials for Li-ion battery. See DOI: 10.1039/c2jm16042k

The synergistic effects between graphene and the secondary phase such as space confinement, electronic modification, and fast charge transfer will also enhance the electrochemical performance of the electrode materials. The applications of graphene-based electrodes for supercapacitor and Li-ion battery use are also highlighted by recent reviews.[8]

To develop graphene-based hybrid electrodes with superior performance in electrochemical energy storage, the selection of appropriate raw materials and the optimization of synthesis strategy are of great importance. Among various approaches for graphene production, the chemically derived graphene (CDG), which uses graphite, graphite oxide (GO) or other graphite derivatives as starting materials, can be produced in large scale, and provides further processability and abundant functions for industrial applications as well.[7,8] Up to now, the reduction of GO to CDGs is the most widely applied technique for the large scale preparation of graphene. During the preparation of graphene-based hybrids, as shown in Fig. 1, the current reported methods can be simply classified into two general strategies according to the processes of CDG synthesis: (1) pre-graphenization strategy: CDG is synthesized (such as thermally reduced graphene (TRG)) before the second component is introduced; (2) post-graphenization strategy: a composite composed of a CDG precursor (usually graphene oxide) and the second component is pre-prepared, followed by converting the precursor into chemical reduced graphene (CRG). Both of them have been widely used for graphene-based hybrid electrode fabrication, but it is still an open question as to which one is better.

To explore an advanced technique as well as reveal the chemical and material science for fabrication of graphene-based electrode materials, SnO_2, which is an important n-type semiconductor with a wide band gap (E_g = 3.6 eV) for many applications such as gas sensors, supercapacitors, and lithium-ion batteries (LiBs), is selected as the secondary component to the graphene supports by pre- or post-graphenization. Recently, SnO_2 has become very attractive as the anode material for the next-generation LiBs because of its high theoretical capacity of 790 mA h g^{-1}. As shown in Fig. 1, both pre-graphenization and post-graphenization process are carried out for SnO_2@graphene hybrid fabrication, and SnO_2@TRG and SnO_2@CRG electrodes are obtained and carefully characterized. Both the graphenes and their hybrids are evaluated for supercapacitors and Li-ion battery electrodes, so as to provide insightful materials chemistry towards development of advanced graphene-based electrodes.

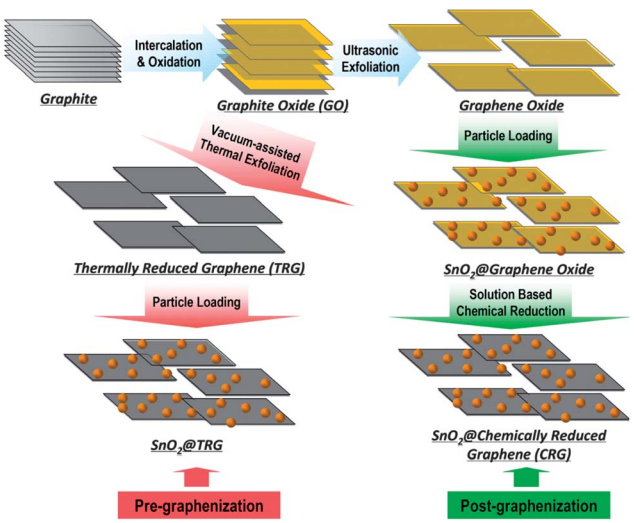

Fig. 1 Illustration of the pre- and post-graphenization route for metal oxide–graphene hybrid fabrication.

2. Experimental

2.1 Pre-graphenization: SnO_2@TRG hybrids

The thermally reduced graphene was obtained by thermal expansion of GO powder under high vacuum. GO was prepared by a modified Hummers method. The as-prepared GO was put into a quartz tube that was sealed at one end and stoppered at the other end, through which the reactor was connected to the high vacuum pump. The tube was heated at a rate of 30 °C min^{-1} under high vacuum (<3.0 Pa). At about 200 °C, an abrupt expansion was observed. To remove the abundant functional groups, the expanded GO was kept at 250 °C for 20 min and a high vacuum was maintained (below 5.0 Pa) during heat treatment. The as-prepared graphene sample was denoted as TRG. The SnO_2@TRG hybrids were prepared by a facile excessive impregnation of the above TRG. In a typical process, 500 mg of TRG was mixed with 500 mL of 0.1 M $SnCl_2$ aqueous solution (with 0.1 M HCl as pH adjuster) in an ice bath (~0 °C). The black mixture was kept in the ice bath with intensive stirring for 10 min, to realize moderate anchoring of Sn^{2+} on the active sites of graphene. The product was isolated by vacuum filtration and rinsed copiously with water (5 × 100 mL) and ethanol (5 × 100 mL). Finally, the sample was air dried at 110 °C for 24 h to obtain SnO_2@TRG hybrids.

2.2 Post-graphenization: SnO_2@CRG hybrids

The CRG was prepared by a chemical reduction approach. In a typical procedure, GO (500 mg) was dispersed in 500 mL water followed by sonication (200 W) for 30 min to yield a homogeneous brown hydrosol of graphene oxide. The above hydrosol was mixed with 50 mL hydrazine monohydrate (NH_2–$NH_2 \cdot H_2O$, 100%) in a 1000 mL round-bottom flask, and heated in an oil bath at 100 °C under a water-cooled condenser for 24 h, during which the reduced GO gradually precipitated out as black solids. The product was isolated by vacuum filtration and washed thoroughly with water and ethanol to remove excessive metal salts. Finally, the sample was air dried in a watch glass at 110 °C for 24 h to obtain chemically reduced graphene. The SnO_2@CRG hybrids were prepared by pre-impregnation of graphene oxide followed by a similar chemical reduction approach. In a typical experimental, 500 mL of graphene oxide hydrosol (1.0 mg mL^{-1}) was pre-mixed with 250 mL of $SnCl_2$ aqueous solution (concentration of 0.32 mg mL^{-1} with 0.10 M HCl as pH adjuster). The mixture was stirred in a ice bath for 10 min, and then moved to an oil bath over which 50 mL of 100% NH_2–$NH_2 \cdot H_2O$ was added gradually. The solution was heated and kept at 100 °C with intensive stirring under a water-cooled condenser for 24 h. The as-prepared products of SnO_2@CRG hybrids are separated, washed and dried using the same method as mentioned above for CRG.

2.3 Sample characterization

The morphologies of the samples were characterized using a Hitachi S4800 scanning electron microscope (SEM) operated at 2.0 kV and a Philips CM200 LaB_6 transmission electron microscope (TEM) operated at 200.0 kV; the HRTEM images of the samples were collected on a FEI Cs-corrected Titan 80-300 microscope operated at 80.0 kV. Energy dispersive X-ray spectroscopy (EDS) analysis was performed using a Titan 80-300 apparatus with the analytical software INCA. The samples were ultrasonically dispersed in ethanol, and then a drop of the solution was deposited on a Lacey carbon film grid to be used for TEM characterization; X-ray diffraction (XRD) measurements were performed at room temperature (Cu K_α radiation, k = 0.15406 nm, D8 Advance, BRUKER/AXS, Germany); X-ray fluorescence (XRF) was employed to analyze the elemental composition of the samples. Before XRF testing, the sample was pre-grinded with wax in ethanol to form a slurry, and then pressed into a pellet with thickness of *ca.* 35 mm; Brunauer–Emmett–Teller (BET) specific surface areas and Barret–Joyner–Halenda (BJH) pore size distributions of the SnO_2–graphene hybrids were determined by N_2 physisorption at 77 K using a Micromeritics 2375 BET apparatus; X-ray photoelectron spectroscopy (XPS) was performed on the Thermo VG ESCALAB250 surface analysis system with parameters: Al Kα = 1486.6 eV, Power = 150 W (HV = 15 kV and I = 10 mA), spot size = 500 lm, pass energy 50.0 eV and energy step size 0.1 eV.

2.4 Supercapacitor performance measurements

The electrochemical properties of graphene–SnO_2 hybrids were measured in an aqueous system (electrolyte: 6.0 M KOH). A three-electrode system was employed in the measurement, whereby Ni foam coated with electrode materials served as the working electrode, a platinum foil electrode as counter electrode and a saturated hydrogen electrode (SHE) served as reference electrode. In order to prepare a working electrode, a mixture of our active material, carbon black, and poly(tetrafluoroethylene) with a weight ratio of 80 : 5 : 15 was ground together to form a homogeneous slurry. The slurry was squeezed into a film and then punched into pellets. The punched pellets with a piece of nickel foam on each side were pressed under 2.5 MPa and dried overnight at 110 °C. Each electrode was quantified to contain roughly 5.0 mg active materials. The electrodes were impregnated with electrolyte under vacuum for 1.0 h prior to the electrochemical evaluation. Cyclic voltammogram (CV) curves (scan rates varying from 3 to 500 mV s^{-1}) and electrochemical impedance spectroscopy (EIS) profiles were measured with a VSP BioLogic electrochemistry workstation. The electrochemical capacitances were both obtained from CV curves. The Nyquist plot was fitted by EC-Lab software.

2.5 Li-ion battery performance measurements

The performances of graphene-based hybrids as anode materials for lithium ion batteries were tested with CR2025 coin cells. A mixture of SnO_2@CRG nanocomposites or SnO_2@TRG, carbon black, and polyvinylidene fluoride at a weight ratio of 80 : 10 : 10 was pasted on pure Cu foil (99.6%, Goodfellow) to make the working electrode. A microporous polyethylene sheet (Celgard 2400) was used as separator. The electrolyte was 1.0 M $LiPF_6$ dissolved in a mixed solution of ethylene carbonate–dimethyl carbonate–ethylene methyl carbonate (1 : 1 : 1, by weight) obtained from Ube Industries Ltd. Pure lithium foil (Aldrich) was used as counter electrode. The cells were assembled in an Ar-filled glove box. The discharge and charge measurements were carried out at different current densities in the voltage range of 0–3.0 V on a Neware battery test system. The specific capacity of the SnO_2@graphene nanocomposites was calculated based on the mass of the anode materials (SnO_2 and graphene). Cyclic voltammogram measurements were performed on a Solartron 1470E electrochemical workstation at a scan rate of 0.1 mV s^{-1}.

3. Results and discussion

3.1 Pre-graphenization: structure of TRG and SnO_2@TRG hybrids

In the pre-graphenization process, the GO is thermally expanded and reduced into a fluffy black powder.[21] As shown in Fig. 2a, the as-obtained TRGs have a hierarchically honeycomb-like morphology: the crumpled graphene sheets with many ripples and wrinkles are loosely stacked or folded with each other to construct a continuous and interconnected 3D macroscopic architecture, with a Brunauer–Emmett–Teller (BET) surface area of ~293 m^2 g^{-1}. The diameter of the macropores ranges from 100 to 300 nm (Fig. 2a and b). The TRG has a coarse edge, which can be attributed to the fast decomposition of oxygen-containing functional groups (such as carboxyl, carbonyl groups) during thermal exfoliation. After the impregnation and calcination process, the pre-graphenized SnO_2@TRG hybrid still holds a porous morphology with twisted and loosely packed graphene sheets. However, the regularity of the ordered honeycomb structure is lost gradually. As the basic building blocks, the

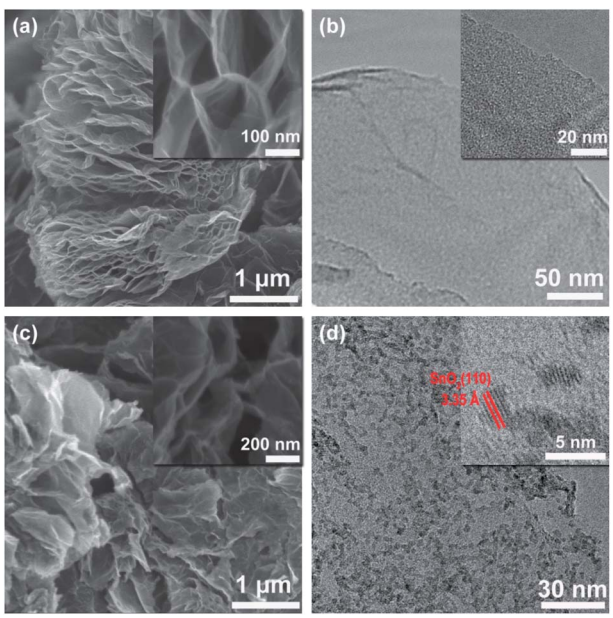

Fig. 2 (a) SEM image of TRG; (b) TEM image of TRG; (c) SEM image of SnO_2@TRG; (d) TEM image of SnO_2@TRG.

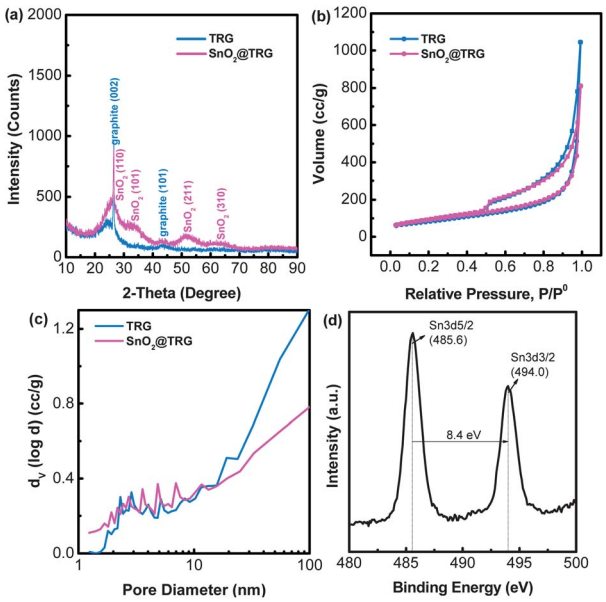

Fig. 3 (a) XRD patterns; (b) N_2 sorption isotherms; (c) BJH adsorption pore size distributions of TRG and SnO_2@TRG; (d) XPS Sn3d fine scan spectrum of SnO_2@TRG.

graphene sheets are larger than 1 μm in diameter, between which pores ranging from 20 to 100 nm are clearly identified (Fig. 2c). The microtexture of SnO_2@TRG was further examined by TEM, SnO_2 nanoparticles with sizes ranging between 3 and 5 nm with a density of *ca.* 4×10^{12} cm^{-2} are formed on the graphene sheets. Some of the SnO_2 particles are agglomerated into chain-like structures. A lattice with a d_{110} space of ~3.35 Å can be clearly demonstrated on the inserted figure of the high resolution TEM images (Fig. 2d), indicating a good crystallization of SnO_2.[15]

The fine scan X-ray diffraction (XRD) spectroscopy (collected at a very slow scan rate of 0.1° min^{-1}) is employed to verify the crystallite structure of pre-graphenized samples. After thermal graphenization, TRG exhibits a tiny sharp peak (002) with a broad shoulder at ~26.6° and a very weak peak (101) at 43.6°, The sharp peak is attributed to the thin-layer graphitic microcrystalline stacking by graphene layers due to inadequate exfoliation of graphite oxide during thermal expansion, while the shoulder is ascribed to the local positive fluctuation of interlayer spacing of graphene layers due to the rotation, translation, curvature and fluctuation of atomic positions along the normal of graphene layers (Fig. 3a).[22] After SnO_2 introduction, despite the carbon related peaks, several very weak peaks around 33.2°, 51.7°, 64.0° emerge, which are assigned to the (101), (211) and (310) lines of the newly formed α-SnO_2 phase, respectively, while the increase in the intensity of the peak and shoulder at ~26.6° is ascribed to a secondary re-stacking of graphene during impregnation and drying, and the amalgamation of the (002) line of graphite with the nearby (110) line of SnO_2. The crystalline size along the (110) lattice ($L_{(110)}$) of SnO_2 is estimated to be ~3.8 nm according to the Scherrer equation, which is consistent with the TEM observation.

The N_2 adsorption–desorption isotherms are carried out to evaluate the change of pore structure for TRG before and after SnO_2 impregnation. As shown in Fig. 2c, both sorption isotherms exhibit the typical Type III isotherm with H3 hysteresis loop according to IUPAC classification, showing materials characteristic of macropores (pore size >50 nm) and comprised of aggregates (loose assemblages) of plate-like particles forming slit-like mesopores (Fig. 3b). The specific BET surface area (S_{BET}), *t*-plot micropore surface area (pore size <2 nm) (S_{micro}), and total pore volume (V_P) of TRG and SnO_2@TRG are summarized in Table 1. After SnO_2 impregnation, the S_{BET} is slightly increased from 293 to 325 m^2 g^{-1}, while the V_P is decreased simultaneously from 1.62 to 1.26 cm^3 g^{-1}, with a corresponding increase of S_{micro} from 6.9 to 12.8 m^2 g^{-1}. The BJH adsorption pore size distribution (Fig. 3c) indicates the key role of exterior meso- and macropores with relatively larger diameters (pore size >2 nm) in contributing the S_{BET} of TRG and SnO_2@TRG, however, the average diameter of the pore is decreasing after the introduction of SnO_2. The evolution of porous structure is attributable to the collapse of exterior macropores due to the capillary effect during solution based impregnation and the air drying process (Fig. 3c).

Furthermore, the XPS results show that the atomic percentages of Sn, C, and O element are 1.71, 85.84, and 12.44 at%, respectively (Table 1). From the fine scan of SnO_2@TRG (Fig. 3d), the Sn components present the typical $3d_{5/2}$ (485.6 eV) and $3d_{3/2}$ (494.0 eV) level with a gap of 8.4 eV and area ratio of ~1.5, which further confirms the state of SnO_2 on TRG.[14]

3.2 Post-graphenization: structure of SnO_2@CRG hybrids

The other route for SnO_2@graphene hybrids is post-graphenization, in which the Sn^{4+} species are grafted onto the surface of GO in advance, and then the chemical transformation from graphene oxide into graphene is conducted by solution based chemical reduction. As shown in Fig. 4a, the CRG exhibits closely packed graphene agglomerates, in which the graphene sheets with high-density ripples and wrinkles are randomly crumpled (Fig. 4b). After SnO_2 addition, the post-graphenized SnO_2@CRG hybrid still holds a highly twisted structure (Fig. 4c), in which only micropores and mesopores are observed. SnO_2 nanoparticles with a density of *ca.* 3×10^{12} cm^2 and

Table 1 Quantification results of BET, XRF and XPS on the TRG, SnO_2@TRG, CRG, and SnO_2@CRG samples

Sample	S_{BET}[a] (m^2 g^{-1})	V_P[a] (m^3 g^{-1})	S_{micro}[a] (m^2 g^{-1})	Bulk. Sn[b] (%)	Surf. Sn[c] (%)	Surf. C[c] (%)	Surf. O[c] (%)
TRG	293	1.62	6.9	0	0.00	89.70	10.30
SnO_2@TRG	325	1.26	12.8	3.86	1.71	85.84	12.44
CRG	666	0.60	69.9	0	0.00	88.43	11.57
SnO_2@CRG	818	1.09	NA	2.00	0.74	88.06	11.21

[a] Calculated by N_2 physisorption. [b] Obtained from XRF. [c] Quantified by XPS.

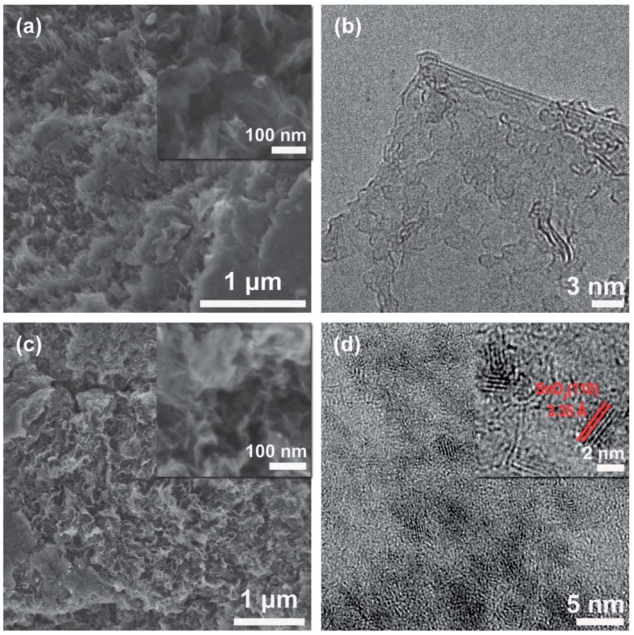

Fig. 4 (a) SEM and (b) TEM images of CRG; (c) SEM and (d) TEM images of SnO_2@CRG.

a diameter of 3.5–5.5 nm are uniformly distributed on the graphene sheets. The lattice of SnO_2 ($d_{110} \sim 3.35$ Å) can be clearly observed on the HRTEM images (Fig. 4d), which implies a high crystallization degree of the SnO_2 particles.

Comparing with the pre-graphenized TRG, CRG exhibits broader and stronger diffraction peaks of the graphite (002) and (101) lattice in the XRD pattern (Fig. 5a), indicating an over re-stacking and entanglement of graphenes within the macro-assembly. However, after introduction of only 2 wt% of Sn components, the graphite associated peaks are significantly minimised with the emersion of very weak SnO_2 peaks, due to the formation of SnO_2 nanocrystals which could further act as the isolation spacers between graphene. Thus, the BET surface area is extended from CRG (666 $m^2 g^{-1}$) to SnO_2@CRG (818 $m^2 g^{-1}$), as more closed pores may become opened ones which are accessible to the N_2 molecules (Table 1).[23]

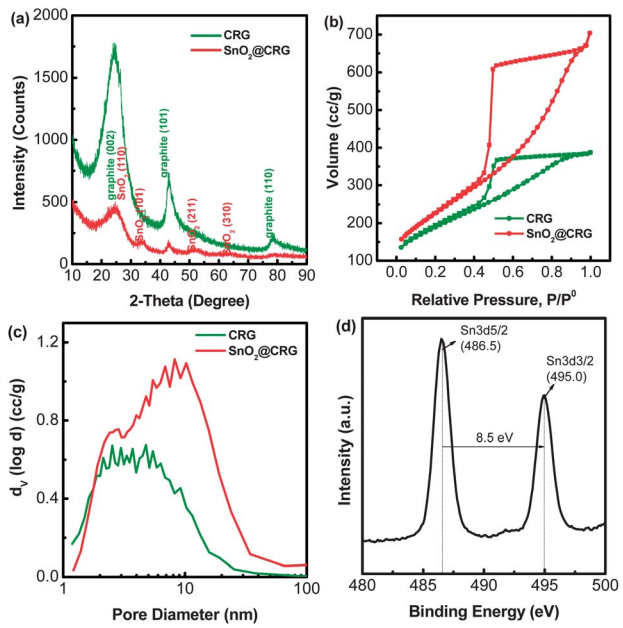

Fig. 5 (a) XRD patterns, (b) N_2 sorption isotherms and (c) BJH adsorption pore size distributions of CRG and SnO_2@CRG; (d) XPS Sn_{3d} fine scan spectrum of SnO_2@CRG.

Furthermore, the N_2 sorption isotherms of both CRG and SnO_2@CRG, as shown in Fig. 5b, present a typical Type IV isotherm with apparent H2 hysteresis loop, indicating the presence of ink-bottle pores between graphene sheets in the architecture. It is noteworthy that the curve of the N_2 sorption isotherm of CRG is apparently different from that of TRG (Fig. 3b and 5b) and there are no macropores in CRG (Fig. 5b). In addition, the S_{BET} of CRG (666 $m^2 g^{-1}$) is higher than that of TRG (293 $m^2 g^{-1}$). These phenomena are mainly attributed to over re-stacking and entanglement of graphenes in CRG materials, generating more mesopores, and to inadequate exfoliation of graphite oxide in TRG. After SnO_2 introduction, the pore volume is increased from 0.60 to 1.09 $cm^3 g^{-1}$ and the vanishing micropore surface area in SnO_2@CRG is observed. The BJH adsorption pore size distribution of CRG and SnO_2@CRG exhibits the parabolic profile with peaks at ~4 and ~10 nm, respectively (Fig. 5c), which is distinct from pre-graphenized SnO_2@TRG samples.

As calculated from XPS, the surface contents of Sn, C, and O on SnO_2@CRG are determined to be 0.74, 88.06, and 11.21 at%, respectively (Table 1). The Sn3d fine scan spectrum exhibits the similar $3d_{5/2}$ and $3d_{3/2}$ line to SnO_2@TRG at 486.5, 495.0 eV with a gap of 8.5 eV, indicating the grafting of SnO_2 on CRG. However, the content of Sn in SnO_2@CRG is much less than that of SnO_2@TRG, as confirmed by XPS and XRF analysis (Table 1).

In the post-graphenization process, due to π–π interaction between graphene sheets, the reduced graphene oxide sheets are likely to be re-stacked into agglomerations in the solution based reduction procedure. Attributing to the removal of negatively charged functional groups, the electrostatic repulsion which keeps the graphene oxide hydrosol stable is decreased.[24] The agglomeration became even more severe due to the capillary attraction effect, as water molecule spacers are spilled out from the graphene interlayer in the final drying process.[25] However, the pre-introduced SnO_2 species on the basal plane of graphene oxide could act as the spacers between graphene so as to prevent the over-compact restacking and agglomeration of graphene during the "wet" process of reduction and drying.

3.3 Electrochemical performance

The SnO_2@TRG and SnO_2@CRG hybrids exhibit distinct microstructures (*e.g.* pore structure, particle loading state, composite interfacial property and functionalities) for their different origin of fabrication processes (pre-graphenization or post-graphenizaton). It would be interesting and meaningful to correlate these structural differences with their electrochemical performance as energy storage materials. Thus, SnO_2@TRG and SnO_2@CRG, with the bare sample TRG and CRG as references, are fabricated and evaluated as electrodes for supercapacitors and Li-ion batteries, respectively.

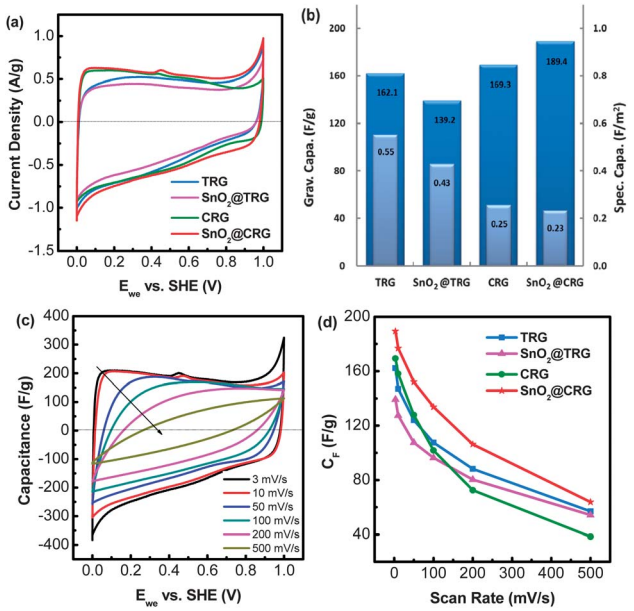

Fig. 6 (a) CV curves and (b) as-calculated C_F and C_S of TRG, SnO_2@TRG, CRG and SnO_2@CRG at 3 mV s^{-1}; (c) CV evolution of SnO_2@CRG with scan rates varies from 3.0 to 500 mV s^{-1}; (d) C_F of four samples at different scan rates from 3.0 to 500 mV s^{-1}.

3.3.1 Supercapacitor. Cyclic voltammetry, electrochemical impedance spectrum, and galvanostatic charge/discharge (GC) techniques are employed to characterize the supercapacitor performance. As shown in Fig. 6a, at a very low scan rate of 3.0 mV s^{-1}, the CV curve of each sample indicates a typical electric double-layer capacitor (EDLC) character. Among them, SnO_2@CRG exhibits a more prominent Faradic redox reaction behavior with relatively lower resistance. Fig. 6c shows the CV characteristics of SnO_2@CRG at different scanning rates, which maintain an EDLC behavior at the higher scan rates of over 200 mV s^{-1}. The gravimetric capacitance (C_F, F g^{-1}) of each electrode at various scan rates is calculated from CV curves and presented in Fig. 6b, while the initial C_F and associated specific capacitance (C_S, F m^{-2}) at 3 mV s^{-1} is shown in Fig. 6d. It is found that the bare samples TRG and CRG exhibit quite a similar capacitance (162.1 F g^{-1} and 169.3 F g^{-1}). However, as the scan rate increases, the value of CRG drops very fast with a final retention of 22.6% at 500 mV s^{-1}, which is significantly lower compared with TRG (35.1% at 500 mV s^{-1}). This phenomenon is in accordance with microstructure and pore structure of thermal/chemical reduced graphene. On one hand, with the exterior porous structure of the assembly and residual surface oxygen functionalities on each basic building block, TRG is endowed with the active surface areas which are highly accessible to the electrolyte. Conversely, the inner surface of ink-bottle pores in CRG, which greatly contribute to the BET surface area, is very difficult to be wetted by the electrolyte. Therefore, though the BET area of TRG (293 m^2 g^{-1}) is significantly smaller than that of CRG (666 m^2 g^{-1}), the specific capacitance per BET area (C_S) of TRG (0.55 F m^{-2}) is remarkably higher than that of CRG (0.25 F m^{-2}). On the other hand, the "open" structure of TRG with numerous large pores could serve as the buffer pool to the electrolyte, thus providing

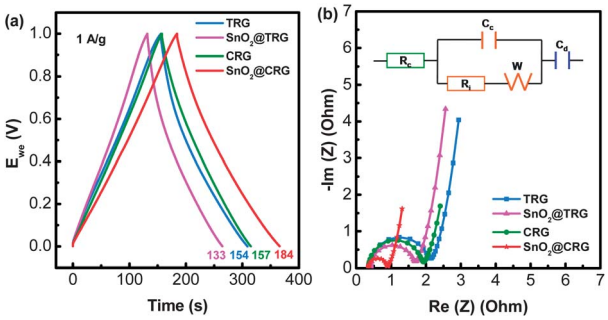

Fig. 7 (a) GC spectrum and (b) Nyquist plots of EIS for TRG, SnO_2@TRG, CRG, and SnO_2@CRG.

a convenient path for ion diffusion between the graphene sheets and electrolyte. Therefore, the TRG electrode exhibits a relatively quicker response in charge/discharge cycling than CRG constructed by over compacted graphene sheets.

The TRG and CRG, after introduction of SnO_2 nano-particles to form the hybrids of SnO_2@TRG and SnO_2@CRG, behave quite differently as supercapacitor electrodes. As shown in Fig. 6d, both the initial C_F at 3 mV s^{-1} and the capacitance retention at higher scan rates of SnO_2@CRG are improved significantly. However, the supercapacitor performance of the SnO_2@TRG electrode is not enhanced as expected, but rather decreased compared with the bare TRG. As a result, the SnO_2@CRG exhibits the highest C_F as a supercapacitor electrode among all the samples, with an initial C_F approaching 189.4 F g^{-1} and retention of 33.7% at 3.0 mV s^{-1}. The controversial effects of SnO_2 hybridization on supercapacitor performance are primarily dependent on the pre- or post-graphenization strategy induced structural difference of the resulting materials.

The GC curves at the current density of 1.0 A g^{-1} are shown in Fig. 7a. All samples exhibit the typical symmetrical charge–discharge patterns of a supercapacitor. In accordance with the capacitances calculated from CV curves, the SnO_2@CRG has the best performance on energy storage among the four samples (184.0 F g^{-1}).

To further confirm the double layer formation of the electrodes, AC impedance spectroscopy is employed to determine the internal components of the devices (Nyquist plots as shown in Fig. 7b). An equivalent circuit model (inset of Fig. 7b) is introduced to simulate the capacitive and resistive elements of the cells under analysis. These elements include the internal resistance of the graphene-based electrode (R_i), the capacitance and resistance due to contact interface (C_c and R_c), a Warburg diffusion element attributable to the ion migration through the graphene (Z_w), and the capacitance inside the pores (C_d).[26] The fitting results are shown in Table 2. In accordance with the synthesis strategy induced structural difference, the as-received SnO_2@graphene hybrids by either pre-graphenization or post-graphenization exhibit a decrease in internal resistance (R_i), due to the increase of charge carrier density in graphene lattice from the electron donor-SnO_2 nano-particles. As a result, SnO_2@CRG has the minimum R_i (0.51 Ω) among the four samples. However, the ion diffusion behavior shows distinct tendency upon SnO_2 decoration by two different graphenization strategies. Compared with TRG (0.71 Ω $s^{-1/2}$), the Warburg diffusion resistance of SnO_2@TRG is increased to

Table 2 Summary of internal components in electrodes

Sample	R_i (Ohm)	R_c (Ohm)	C_c (F g^{-1})	W (Ohm s$^{-1/2}$)	C_d (F g^{-1})
TRG	1.65	0.40	0.27	0.71	170.51
SnO_2@TRG	1.22	0.41	0.15	0.74	145.72
CRG	1.50	0.36	0.12	0.45	226.07
SnO_2@CRG	0.51	0.36	0.09	0.36	232.53

0.74 Ω s$^{-1/2}$, which is ascribed to the collapse of some honeycomb-like structures during the impregnation and drying process. Conversely, the value for SnO_2@CRG (0.36 Ω s$^{-1/2}$) is smaller than that of CRG (0.45 Ω s$^{-1/2}$), which is attributed to the prominent "spacer" effect of SnO_2 nano-particles. Thereafter, from a viewpoint of thermodynamics, the mass transfer within the electrochemical system is significantly promoted through: (i) improvement of charge transfer along the graphene lattice and between graphene by π–π interactions of delocalized electrons arising from both graphitic domains and SnO_2 electron donors; and (ii) optimization of the porous structure by preventing the re-stacking of graphene so as to offer a low resistance channel for ion diffusion. Thus, the PC-active SnO_2 species combining with the graphene surface inside the pores of SnO_2@CRG are highly accessible to the ions of electrolyte, so as to give rise to capacitance inside pores with a maximum value of as high as 232.53 F g^{-1} among the four samples.

3.3.2 Li-ion battery. SnO_2 shows a high theoretical capacity of Li^+ intercalations–deintercalations (790 mA h g^{-1}), which makes it a promising anode material for Li-ion batteries. Fig. 8 shows the representative CVs of the sample. Specifically, two pairs of redox current peaks can be clearly observed. The first dominant pair (cathodic, anodic) shown at the potential (V) of (0.01, 0.7) can be attributed to the alloying (cathodic scan) and dealloying (anodic scan) processes. The first pair is much more pronounced than the second pair, marking its major contribution to the total capacity of the cell. The intensity of this pair of SnO_2@TRG is much higher than that of SnO_2@CRG, which is attributed to higher loading of SnO_2 on TRG (2.17%) than that on CRG (0.94%). The second pair at (0.65, 1.3) is mainly appeared on the SnO_2@TRG electrode. This pair of redox peaks is related to the irreversible reduction of SnO_2 to Sn, which disappeared in the second cycle. Comparing the second cycle to

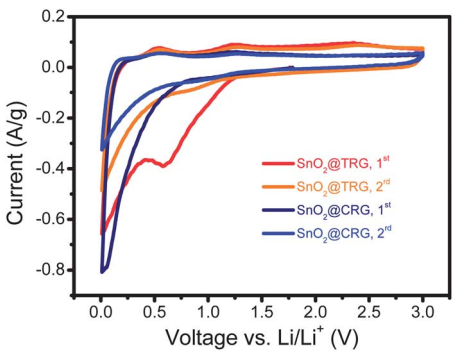

Fig. 8 The cyclic voltammogram of the SnO_2@T/CRG nanocomposite at a scan rate of 0.1 mV s^{-1}.

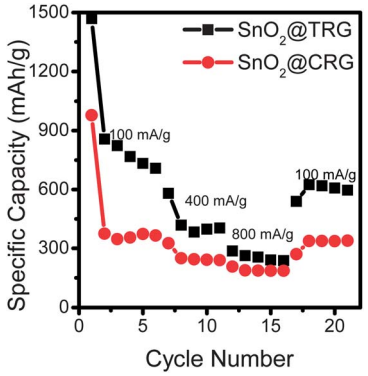

Fig. 9 The discharge capacity at different charge/discharge current rates for SnO_2@TRG and SnO_2@CRG nanocomposites.

the first one, the decreased intensity is mainly attributed to the reaction of oxygen-containing functional groups on graphene with lithium ions and the formation of a surface polymeric layer due to the decomposition of the solvent in the electrolyte.

The rate performances of SnO_2@TRG and SnO_2@CRG are demonstrated in Fig. 9. The discharge capacities in the 1st cycle are 1468 mA h g^{-1} for SnO_2@TRG, and 978 mA h g^{-1} for SnO_2@CRG. The formation of solid electrolyte interface (SEI) is the main reason that caused the large capacity and also the irreversible capacity loss. For the 2nd cycle, the discharge capacities are 857 mA h g^{-1} for SnO_2@TRG, and 375 mA h g^{-1} for SnO_2@CRG. The discharge capacities in the 6th cycle are 707 mA h g^{-1} for SnO_2@TRG with a coulombic efficiency of 90%, and 366 mA h g^{-1} for SnO_2@CRG with a coulombic efficiency of 94%. With higher current density during the galvanostatic discharge (Li insertion, voltage decreases)/charge (Li extraction, voltage increases) process, the discharge capacity further decreased. The discharge capacities in the 7th cycle (current density at 400 mA g^{-1}) are 580 mA h g^{-1} for SnO_2@TRG, and 366 mA h g^{-1} for SnO_2@CRG. Further increase of charge and discharge current to 800 mA g^{-1} caused the drop of capacity of SnO_2@TRG and SnO_2@CRG to 286 and 206 mA h g^{-1}, respectively. Upon returning back to a low current density of 100 mA g^{-1}, the discharge capacities for SnO_2@TRG and SnO_2@CRG recovered to 540 and 271 mA h g^{-1} at the 17th cycle. Comparing the performance of TRG and CRG (Fig. S1†), the addition of SnO_2 acted as spacer for the CRG sample, but a filler in the TGR pores. The graphene electrode afforded the main characteristics of Li storage for the current hybrid electrode. Compared with the CRG electrode, improved Li storage performance for SnO_2@CRG was presented; while the discharging capacity of SnO_2@TRG was not as high as that of pure TRG anode materials.

The cycling performances of SnO_2@graphene composite and pure graphene anode materials are presented in Fig. 10 and S2†, respectively. With a charge/discharge current density at 400 mA g^{-1}, SnO_2@TRG and SnO_2@CRG composites show discharge capacities of 204 and 196 mA h g^{-1} even after 100 cycles (Fig. 10). A rapid capacity loss can be observed during the initial three cycles for SnO_2@CRG and CRG. In contrast, a gradual loss occurred on SnO_2@TRG and TRG. The higher initial discharge capacity of the SnO_2@TRG composite can be attributed to its loading amount of SnO_2 as shown in Table 1.

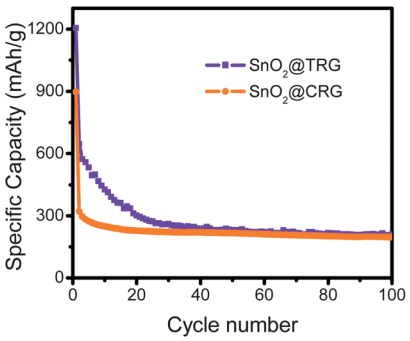

Fig. 10 The discharge capacity *vs.* cycle number for SnO_2@TRG and SnO_2@CRG at a charge–discharge current of 400 mA g^{-1}.

However, because of the unstable porous structure and complex surface chemistry, the high capacity of both SnO_2@TRG and TRG is not well maintained. This indicated that pre-graphenization provides huge surface area for more metal oxide anchoring, while such a porous TRG is not very stable. In contrast, the post-graphenization process provides more anchoring sites for the formation of a large number of small SnO_2 particles, and the as-obtained SnO_2@CRG shows a more stable behavior as an anode material.

4. Conclusions

To clarify the effect of pre- or post-graphenization for graphene-based hybrids, two kinds of SnO_2@graphene hybrids are explored with the same GO and Sn precursors. For the pre-graphenization strategy: the thermally reduced graphene is obtained before the second component (SnO_2) is introduced; for the post-graphenization strategy: a composite composed of graphene oxide and the second component (SnO_2) is pre-prepared, followed by converting the precursor into chemically reduced graphene. The SnO_2 nanoparticles with a loading of 6.3 wt% are distributed on porous TRG, while a loading of 3.3 wt% was determined on compacted CRG. When the SnO_2@graphene is used as a supercapacitor electrode, the SnO_2@CRG exhibits the highest C_F as a supercapacitor electrode among all the samples with an initial C_F approaching 189.4 F g^{-1} and retention of 33.7% at 3.0 mV s^{-1}. The gravimetric capacitance of CRG drops very fast with a final retention of 22.6% at 500 mV s^{-1}, which is significantly lower compared with TRG (35.1% at 500 mV s^{-1}). When they are employed as Li-ion battery electrodes, the discharge capacities in the 1st cycle are 1468 and 978 mA h g^{-1} for SnO_2@TRG and SnO_2@CRG, respectively. With higher current density during the galvanostatic discharge (Li insertion, voltage decreases)/charge (Li extraction, voltage increases) process, the discharge capacities of both SnO_2@TRG and SnO_2@CRG decreased gradually. Even after 100 cycles at 400 mA g^{-1}, a discharging capacity of 204 and 196 mA h g^{-1} can still be retained for SnO_2@TRG and SnO_2@CRG, respectively. This suggested that the method of graphenization provides the hybrid with different structure and electrochemical performance. The pre-graphenization process provides a large amount of pores for ion diffusion, which is of benefit for loading of SnO_2, fast ion diffusion for supercapacitors, and higher capacity for Li-ion batteries, but poor stability, while the post-graphenization process offers compact graphene and good interaction between the SnO_2 and graphene, which provides stable structure for long term stability for supercapacitor and Li-ion battery use. The optimized graphenization method for graphene hybrids should be further explored to provide new insights into hybrid formation and advanced materials for energy storage.

Acknowledgements

The authors greatly appreciate financial support by the Ener-Chem project of the Max Planck Society. The authors gratefully acknowledge Gisela Lorenz, Frank Gigelis, and Edith Kitzelmann for kindly help. C.M.C. and X.C.Z. also appreciate the sponsorship from the "CAS-MPG Joint PhD Promotion Programme 2010".

Notes and references

1 E. Frackowiak and F. Beguin, *Carbon*, 2001, **39**, 937.
2 J. Yan, Z. J. Fan, T. Wei, W. Z. Qian, M. L. Zhang and F. Wei, *Carbon*, 2010, **48**, 3825.
3 A. S. Arico, P. Bruce, B. Scrosati, J. M. Tarascon and W. Van Schalkwijk, *Nat. Mater.*, 2005, **4**, 366; P. G. Bruce, B. Scrosati and J. M. Tarascon, *Angew. Chem., Int. Ed.*, 2008, **47**, 2930; N. A. Kaskhedikar and J. Maier, *Adv. Mater.*, 2009, **21**, 2664.
4 D. S. Su and R. Schlogl, *ChemSusChem*, 2010, **3**, 136; C. Liu, F. Li, L. P. Ma and H. M. Cheng, *Adv. Mater.*, 2010, **22**, E28.
5 C. H. Huang, R. A. Doong, D. Gu and D. Y. Zhao, *Carbon*, 2011, **49**, 3055; C.-H. Huang and R.-A. Doong, *Microporous Mesoporous Mater.*, 2012, **147**, 47.
6 Q. Zhang, J. Q. Huang, M. Q. Zhao, W. Z. Qian and F. Wei, *ChemSusChem*, 2011, **4**, 864.
7 Y. W. Zhu, S. Murali, W. W. Cai, X. S. Li, J. W. Suk, J. R. Potts and R. S. Ruoff, *Adv. Mater.*, 2010, **22**, 3906; H. Bai, C. Li and G. Q. Shi, *Adv. Mater.*, 2011, **23**, 1089.
8 S. J. Guo and S. J. Dong, *Chem. Soc. Rev.*, 2011, **40**, 2644; Y. Q. Sun, Q. O. Wu and G. Q. Shi, *Energy Environ. Sci.*, 2011, **4**, 1113.
9 M. H. Liang and L. J. Zhi, *J. Mater. Chem.*, 2009, **19**, 5871; Y. H. Hu, H. Wang and B. Hu, *ChemSusChem*, 2010, **3**, 782; C. N. R. Rao, A. K. Sood, K. S. Subrahmanyam and A. Govindaraj, *Angew. Chem., Int. Ed.*, 2009, **48**, 7752.
10 Y. Zhu, S. Murali, W. Cai, X. Li, J. W. Suk, J. R. Potts and R. S. Ruoff, *Adv. Mater.*, 2010, **22**, 3906.
11 Z. J. Fan, J. Yan, T. Wei, L. J. Zhi, G. Q. Ning, T. Y. Li and F. Wei, *Adv. Funct. Mater.*, 2011, **21**, 2366; Q. Cheng, J. Tang, J. Ma, H. Zhang, N. Shinya and L. C. Qin, *Carbon*, 2011, **49**, 2917.
12 S. B. Yang, G. L. Cui, S. P. Pang, Q. Cao, U. Kolb, X. L. Feng, J. Maier and K. Mullen, *ChemSusChem*, 2010, **3**, 236; H. Kim, D. H. Seo, S. W. Kim, J. Kim and K. Kang, *Carbon*, 2010, **49**, 326; S. B. Yang, X. L. Feng, S. Ivanovici and K. Mullen, *Angew. Chem., Int. Ed.*, 2010, **49**, 8408.
13 H. Liu, G. X. Wang, J. Liu, S. Z. Qiao and H. J. Ahn, *J. Mater. Chem.*, 2011, **21**, 3046.
14 F. H. Li, J. F. Song, H. F. Yang, S. Y. Gan, Q. X. Zhang, D. X. Han, A. Ivaska and L. Niu, *Nanotechnology*, 2009, **20**, 455602; L. S. Zhang, L. Y. Jiang, H. J. Yan, W. D. Wang, W. Wang, W. G. Song, Y. G. Guo and L. J. Wan, *J. Mater. Chem.*, 2010, **20**, 5462.
15 S. M. Paek, E. Yoo and I. Honma, *Nano Lett.*, 2009, **9**, 72.
16 J. Yao, X. P. Shen, B. Wang, H. K. Liu and G. X. Wang, *Electrochem. Commun.*, 2009, **11**, 1849; H. Kim, S. W. Kim, Y. U. Park, H. Gwon, D. H. Seo, Y. Kim and K. Kang, *Nano Res.*, 2010, **3**, 813; Y. M. Li, X. J. Lv, J. Lu and J. H. Li, *J. Phys. Chem. C*, 2010, **114**, 21770; X. D. Huang, X. F. Zhou, L. A. Zhou, K. Qian, Y. H. Wang, Z. P. Liu and C. Z. Yu, *ChemPhysChem*, 2011, **12**, 278; P. C. Lian, X. F. Zhu, S. Z. Liang, Z. Li, W. S. Yang and H. H. Wang, *Electrochim. Acta*, 2011, **56**, 4532; H. J. Song, L. C. Zhang, C. L. He, Y. Qu, Y. F. Tian and Y. Lv, *J. Mater. Chem.*, 2011, **21**, 5972; X. Y. Wang, X. F. Zhou, K. Yao, J. G. Zhang and Z. P. Liu, *Carbon*, 2011, **49**, 133; M. Zhang, D. Lei, Z. F. Du, X. M. Yin, L. B. Chen, Q. H. Li, Y. G. Wang and T. H. Wang, *J. Mater. Chem.*, 2011, **21**, 1673.

17 J. Z. Wang, C. Zhong, D. Wexler, N. H. Idris, Z. X. Wang, L. Q. Chen and H. K. Liu, *Chem.–Eur. J.*, 2011, **17**, 661.
18 K. Zhang, L. L. Zhang, X. S. Zhao and J. S. Wu, *Chem. Mater.*, 2010, **22**, 1392; X. C. Zhao, A. Q. Wang, J. W. Yan, G. Q. Sun, L. X. Sun and T. Zhang, *Chem. Mater.*, 2010, **22**, 5463.
19 A. R. Liu, C. Li, H. Bai and G. Q. Shi, *J. Phys. Chem. C*, 2010, **114**, 22783.
20 Z. J. Fan, J. Yan, L. J. Zhi, Q. Zhang, T. Wei, J. Feng, M. L. Zhang, W. Z. Qian and F. Wei, *Adv. Mater.*, 2010, **22**, 3723.
21 W. Lv, D. M. Tang, Y. B. He, C. H. You, Z. Q. Shi, X. C. Chen, C. M. Chen, P. X. Hou, C. Liu and Q. H. Yang, *ACS Nano*, 2009, **3**, 3730.
22 Z. Q. Li, C. J. Lu, Z. P. Xia, Y. Zhou and Z. Luo, *Carbon*, 2007, **45**, 1686.
23 M. Inagaki, *New Carbon Mater.*, 2009, **24**, 193.
24 L. J. Cote, F. Kim and J. Huang, *J. Am. Chem. Soc.*, 2009, **131**, 1043; J. Kim, L. J. Cote, F. Kim, W. Yuan, K. R. Shull and J. X. Huang, *J. Am. Chem. Soc.*, 2010, **132**, 8180.
25 X. Yang, J. Zhu, L. Qiu and D. Li, *Adv. Mater.*, 2011, **23**, 2833.
26 G. H. Xu, C. Zheng, Q. Zhang, J. Q. Huang, M. Q. Zhao, J. Q. Nie, X. H. Wang and F. Wei, *Nano Res.*, 2011, **4**, 870; C. W. Huang, C. H. Hsu, P. L. Kuo, C. T. Hsieh and H. S. Teng, *Carbon*, 2011, **49**, 895.